Reparameterized Tensor Ring Functional Decomposition for Multi-Dimensional Data Recovery

Supplementary Material

This supplementary material provides additional technical details and experimental results. In Section A, we present the complete proofs of all theorems in the main paper. Section B describes the model configurations and parameter settings used for the four tasks. Section C reports extended experiments, including ablation studies and practical applications.

A. Detaied Proofs of Theorems

Theorem 1. *Let $\mathcal{X} = \Phi(\mathcal{G}^{(1)}, \ldots, \mathcal{G}^{(d)})$ be a TR decomposition. Suppose that the mode-2 frequency components of $\mathcal{G}^{(k)}$ beyond a threshold Ω_k are negligible for all k, i.e.,*

$$\|\big(\mathscr{F}_2[\mathcal{G}^{(k)}]\big)_{:\omega_k:}\|_\infty \le \epsilon,\ \forall|\omega_k| > \Omega_k, k = 1, 2, \ldots, d,$$

where $\epsilon > 0$ is a small constant. Then the reconstructed tensor $\mathcal{X}$ also exhibits attenuated high-frequency content along mode k:

$$\|\big(\mathscr{F}_k[\mathcal{X}]\big)_{:\omega_k:}\|_\infty \le c_k\,\epsilon,\ \forall|\omega_k| > \Omega_k, k = 1, 2, \ldots, d,$$

where c_k is a constant depending only on the magnitudes of the remaining cores $\{\mathcal{G}^{(j)}\}_{j\neq k}$.

Proof. In TR decomposition, each element of $\mathcal{X}$ is expressed as

$$\mathcal{X}_{v_1,\ldots,v_d} = \mathrm{trace}\Big(\mathcal{G}^{(1)}_{:v_1:}\mathcal{G}^{(2)}_{:v_2:}\cdots\mathcal{G}^{(k)}_{:v_k:}\cdots\mathcal{G}^{(d)}_{:v_d:}\Big).$$

By the cyclic property of the trace, we can isolate the k-th factor:

$$\mathcal{X}_{v_1,\ldots,v_d} = \mathrm{trace}\Big(\mathbf{M}_{(\neg k)}\cdot\mathcal{G}^{(k)}_{:v_k:}\Big),$$

where

$$\mathbf{M}_{(\neg k)} = \mathcal{G}^{(k+1)}_{:v_{k+1}:}\cdots\mathcal{G}^{(d)}_{:v_d:}\mathcal{G}^{(1)}_{:v_1:}\cdots\mathcal{G}^{(k-1)}_{:v_{k-1}:} \in \mathbb{R}^{r_{k+1}\times r_k}.$$

For fixed indices $\{v_j\}_{j\neq k}$, the matrix $\mathbf{M}_{(\neg k)}$ is constant with respect to v_k. Expanding the trace gives

$$\mathcal{X}_{v_1,\ldots,v_d} = \sum_{p=1}^{r_k}\sum_{q=1}^{r_{k+1}}[\mathbf{M}_{(\neg k)}]_{q,p}\,\mathcal{G}^{(k)}_{p,v_k,q}.$$

Applying the mode-k DFT along the k-th dimension, we obtain

$$\begin{aligned}
&\big(\mathscr{F}_k[\mathcal{X}]\big)_{v_1,\ldots,\omega_k,\ldots,v_d}\\
&= \sum_{v_k=1}^{n_k}\mathcal{X}_{v_1,\ldots,v_k,\ldots,v_d}\cdot[\mathbf{F}_k]_{v_k,\omega_k}\\
&= \sum_{v_k=1}^{n_k}\left(\sum_{p=1}^{r_k}\sum_{q=1}^{r_{k+1}}[\mathbf{M}_{(\neg k)}]_{q,p}\cdot\mathcal{G}^{(k)}_{p,v_k,q}\right)\cdot[\mathbf{F}_k]_{v_k,\omega_k}\\
&= \sum_{p=1}^{r_k}\sum_{q=1}^{r_{k+1}}[\mathbf{M}_{(\neg k)}]_{q,p}\cdot\left(\sum_{v_k=1}^{n_k}\mathcal{G}^{(k)}_{p,v_k,q}\cdot[\mathbf{F}_k]_{v_k,\omega_k}\right).
\end{aligned}$$

Using the definition of mode-2 DFT for the TR factor $\mathcal{G}^{(k)}$,

$$\big(\mathscr{F}_2[\mathcal{G}^{(k)}]\big)_{p,\omega_k,q} = \sum_{v_k=1}^{n_k}\mathcal{G}^{(k)}_{p,v_k,q}\cdot[\mathbf{F}_k]_{v_k,\omega_k},$$

we can rewrite the expression as

$$\begin{aligned}
&\big(\mathscr{F}_k[\mathcal{X}]\big)_{v_1,\ldots,\omega_k,\ldots,v_d}\\
&= \sum_{p=1}^{r_k}\sum_{q=1}^{r_{k+1}}[\mathbf{M}_{(\neg k)}]_{q,p}\cdot\big(\mathscr{F}_2[\mathcal{G}^{(k)}]\big)_{p,\omega_k,q}.
\end{aligned}$$

We now bound the magnitude of this term. Using the triangle inequality:

$$\begin{aligned}
&\Big|\big(\mathscr{F}_k[\mathcal{X}]\big)_{v_1,\ldots,\omega_k,\ldots,v_d}\Big|\\
&\le \sum_{p=1}^{r_k}\sum_{q=1}^{r_{k+1}}\big|[\mathbf{M}_{(\neg k)}]_{q,p}\big|\cdot\Big|\big(\mathscr{F}_2[\mathcal{G}^{(k)}]\big)_{p,\omega_k,q}\Big|.
\end{aligned}$$

By the assumption on $\mathcal{G}^{(k)}$, for all $|\omega_k| > \Omega_k$, we have

$$\Big|\big(\mathscr{F}_2[\mathcal{G}^{(k)}]\big)_{p,\omega_k,q}\Big| \le \epsilon.$$

Substituting this bound:

$$\Big|\big(\mathscr{F}_k[\mathcal{X}]\big)_{v_1,\ldots,\omega_k,\ldots,v_d}\Big| \le \epsilon\cdot\left(\sum_{p=1}^{r_k}\sum_{q=1}^{r_{k+1}}\big|[\mathbf{M}_{(\neg k)}]_{q,p}\big|\right).$$

Defining the constant c_k as the maximum possible sum of magnitudes of the product of the remaining cores:

$$c_k := \max_{\{v_j\}_{j\neq k}}\sum_{p=1}^{r_k}\sum_{q=1}^{r_{k+1}}\big|[\mathbf{M}_{(\neg k)}]_{q,p}\big|,$$

we obtain the final bound for the infinity norm over the spatial indices $\{v_j\}_{j\neq k}$:

$$\|\big(\mathscr{F}_k[\mathcal{X}]\big)_{:\omega_k:}\|_\infty \le c_k\,\epsilon,\quad \forall|\omega_k| > \Omega_k.$$

This completes the proof. □

Theorem 2. *Consider a TR factor $\mathcal{G}$ reparameterized as $\mathcal{G} = \mathcal{C} \times_3 \mathbf{B}$, where $\mathcal{C} \in \mathbb{R}^{r_1 \times n \times R_2}$ is a trainable tensor and $\mathbf{B} \in \mathbb{R}^{r_2 \times R_2}$ is a fixed basis. Let $\mathsf{L}(\omega)$ be the loss associated with frequency ω. For any $\omega_{\text{high}} > \omega_{\text{low}} > 0$, given any $\epsilon \geq 0$, and fixed indices p, q with $1 \leq p \leq r_1$ and $1 \leq q \leq n$, there exists a matrix $\mathbf{B}$ such that for all $s = 1, \ldots, R_2$,*

$$\left| \frac{\partial \mathsf{L}(\omega_{\text{high}})}{\partial \mathcal{C}_{pqs}} \Big/ \frac{\partial \mathsf{L}(\omega_{\text{low}})}{\partial \mathcal{C}_{pqs}} \right| \geq \max_{j=1,\ldots,r_2} \left| \frac{\partial \mathsf{L}(\omega_{\text{high}}))}{\partial \mathcal{G}_{pqj}} \Big/ \frac{\partial \mathsf{L}(\omega_{\text{low}})}{\partial \mathcal{G}_{pqj}} \right| - \epsilon.$$

Proof. First, from the reparameterization $\mathcal{G} = \mathcal{C} \times_3 \mathbf{B}$, we have

$$\mathcal{G}_{pqj} = \sum_{s=1}^{R_2} \mathcal{C}_{pqs} \mathbf{B}_{js},$$

Viewing $\mathcal{G}_{pq1}, \ldots, \mathcal{G}_{pqr_2}$ as latent variables dependent on $\mathcal{C}_{pqs}$, by the chain rule we obtain

$$\frac{\partial \mathsf{L}(\omega)}{\partial \mathcal{C}_{pqs}} = \sum_{t=1}^{r_2} \frac{\partial \mathsf{L}(\omega)}{\partial \mathcal{G}_{pqt}} \mathbf{B}_{ts}.$$

Next, given two frequencies $\omega_{\text{high}} > \omega_{\text{low}} > 0$ and fixed fiber indices p, q, define

$$\tau = \operatorname*{argmax}_j \left| \frac{\partial \mathsf{L}(\omega_{\text{high}}))}{\partial \mathcal{G}_{pqj}} \Big/ \frac{\partial \mathsf{L}(\omega_{\text{low}})}{\partial \mathcal{G}_{pqj}} \right|.$$

By the triangle inequality, we have

$$\begin{aligned}
&\left| \frac{\partial \mathsf{L}(\omega_{\text{high}})}{\partial \mathcal{C}_{pqs}} \Big/ \frac{\partial \mathsf{L}(\omega_{\text{low}})}{\partial \mathcal{C}_{pqs}} \right| \\
&= \left| \frac{\frac{\partial \mathsf{L}(\omega_{\text{high}})}{\partial \mathcal{G}_{pq\tau}} \mathbf{B}_{\tau s} + \sum_{t \neq \tau} \frac{\partial \mathsf{L}(\omega_{\text{high}})}{\partial \mathcal{G}_{pqt}} \mathbf{B}_{ts}}{\frac{\partial \mathsf{L}(\omega_{\text{low}})}{\partial \mathcal{G}_{pq\tau}} \mathbf{B}_{\tau s} + \sum_{t \neq \tau} \frac{\partial \mathsf{L}(\omega_{\text{low}})}{\partial \mathcal{G}_{pqt}} \mathbf{B}_{ts}} \right| \\
&\geq \frac{\left| \frac{\partial \mathsf{L}(\omega_{\text{high}})}{\partial \mathcal{G}_{pq\tau}} \mathbf{B}_{\tau s} \right| - \left| \sum_{t \neq \tau} \frac{\partial \mathsf{L}(\omega_{\text{high}})}{\partial \mathcal{G}_{pqt}} \mathbf{B}_{ts} \right|}{\left| \frac{\partial \mathsf{L}(\omega_{\text{low}})}{\partial \mathcal{G}_{pq\tau}} \mathbf{B}_{\tau s} \right| + \left| \sum_{t \neq \tau} \frac{\partial \mathsf{L}(\omega_{\text{low}})}{\partial \mathcal{G}_{pqt}} \mathbf{B}_{ts} \right|}.
\end{aligned}$$

For the elements of $\mathbf{B}$, construct $\mathbf{B}_{ts}$ such that for $s = 1, \ldots, R_2$, $|\mathbf{B}_{ts}| \leq \alpha$ when $t \neq \tau$ and $\mathbf{B}_{\tau s} = 1$, where $\alpha > 0$ is a positive upper bound. Define

$$M_1 = \sum_{t \neq \tau} \left| \frac{\partial \mathsf{L}(\omega_{\text{high}})}{\partial \mathcal{G}_{pqt}} \right|, \quad M_2 = \sum_{t \neq \tau} \left| \frac{\partial \mathsf{L}(\omega_{\text{low}})}{\partial \mathcal{G}_{pqt}} \right|.$$

Without loss of generality, for any $\epsilon \geq 0$, choose

$$\alpha \leq \min \left\{ \frac{\left| \frac{\partial \mathsf{L}(\omega_{\text{low}})}{\partial \mathcal{G}_{pq\tau}} \right| \epsilon}{M_1 + M_2 \left| \frac{\partial \mathsf{L}(\omega_{\text{high}})}{\partial \mathcal{G}_{pq\tau}} \Big/ \frac{\partial \mathsf{L}(\omega_{\text{low}})}{\partial \mathcal{G}_{pq\tau}} \right| - M_2 \epsilon}, \frac{1}{M_1} \left| \frac{\partial \mathsf{L}(\omega_{\text{high}})}{\partial \mathcal{G}_{pq\tau}} \right| \right\}.$$

From the upper bound on α, it holds that

$$\left| \sum_{t \neq \tau} \frac{\partial \mathsf{L}(\omega_{\text{high}})}{\partial \mathcal{G}_{pqt}} \mathbf{B}_{ts} \right| \leq \alpha M_1 \leq \left| \frac{\partial \mathsf{L}(\omega_{\text{high}})}{\partial \mathcal{G}_{pq\tau}} \right|,$$

which implies

$$\left| \frac{\partial \mathsf{L}(\omega_{\text{high}})}{\partial \mathcal{G}_{pq\tau}} \right| - \left| \sum_{t \neq \tau} \frac{\partial \mathsf{L}(\omega_{\text{high}})}{\partial \mathcal{G}_{pqt}} \mathbf{B}_{ts} \right| \geq 0.$$

Thus, for fixed p, q and for $s = 1, \ldots, R_2$, we get

$$\begin{aligned}
&\left| \frac{\partial \mathsf{L}(\omega_{\text{high}})}{\partial \mathcal{C}_{pqs}} \Big/ \frac{\partial \mathsf{L}(\omega_{\text{low}})}{\partial \mathcal{C}_{pqs}} \right| \\
&\geq \frac{\left| \frac{\partial \mathsf{L}(\omega_{\text{high}})}{\partial \mathcal{G}_{pq\tau}} \right| - \alpha M_1}{\left| \frac{\partial \mathsf{L}(\omega_{\text{low}})}{\partial \mathcal{G}_{pq\tau}} \right| + \alpha M_2} \\
&\geq \frac{\left| \frac{\partial \mathsf{L}(\omega_{\text{high}})}{\partial \mathcal{G}_{pq\tau}} \right| - \epsilon \left| \frac{\partial \mathsf{L}(\omega_{\text{low}})}{\partial \mathcal{G}_{pq\tau}} \right|}{\left| \frac{\partial \mathsf{L}(\omega_{\text{low}})}{\partial \mathcal{G}_{pq\tau}} \right|} \\
&= \max_{j=1,\ldots,r_2} \left| \frac{\partial \mathsf{L}(\omega_{\text{high}}))}{\partial \mathcal{G}_{pqj}} \Big/ \frac{\partial \mathsf{L}(\omega_{\text{low}})}{\partial \mathcal{G}_{pqj}} \right| - \epsilon.
\end{aligned}$$

The second inequality is obtained by applying the first upper bound of α. This completes the proof. □

Remark. *We note that the proof of Theorem 2 provides an existence guarantee, demonstrating that a suitable choice of $\mathbf{B}$ can in principle amplify high-frequency gradients. However, the specific construction in the proof is not employed in practice, as the optimal index τ is dynamic and depends on the data, making it infeasible to pre-specify. Instead, we adopt the principled Xavier-style initialization described in Theorem 3, which preserves variance in both forward and backward passes. This provides a stable starting point for optimization while allowing the model to learn from a fully expressive random state.*

Theorem 3. *Suppose the entries of $\mathbf{B}^{(k)}$ in the reparameterized TR factor are sampled independently from a uniform distribution as*

$$\mathbf{B}_{ij}^{(k)} \sim \mathcal{U}\left(-\sqrt{\frac{6}{r_{k+1} + R_{k+1}}}, \sqrt{\frac{6}{r_{k+1} + R_{k+1}}} \right), \forall i, j, k,$$

then the variances in both the forward and backward passes are preserved.

Proof. We derive the variance of the initialization parameter $\sigma_{\mathbf{B}}^2$ by enforcing variance preservation in both the forward and backward passes.

Forward pass. Each element of $\mathcal{G}^{(k)}$ is computed as

$$\mathcal{G}_{pqj}^{(k)} = \sum_{s=1}^{R_{k+1}} \mathcal{C}_{pqs}^{(k)} \mathbf{B}_{js}^{(k)}.$$

Since both $\mathcal{C}^{(k)}$ and $\mathbf{B}^{(k)}$ are zero-mean and independent, the variance of $\mathcal{G}_{pqj}^{(k)}$ is

$$\operatorname{Var}(\mathcal{G}_{pgj}^{(k)}) = R_{k+1} \sigma_{\mathcal{C}}^2 \sigma_{\mathbf{B}}^2.$$

To maintain signal variance, we require that

$$\mathrm{Var}(\mathcal{G}^{(k)}_{pgj}) = \mathrm{Var}(\mathcal{C}^{(k)}_{pqj}) = \sigma^2_{\mathcal{C}},$$

which gives

$$\sigma^2_{\mathbf{B}} = \frac{1}{\hat{R}_{i+1}}.$$

Backward pass. During backpropagation, the gradient of the loss function with respect to $\mathcal{C}^{(k)}_{pqj}$ is

$$\frac{\partial \mathsf{L}}{\partial \mathcal{C}^{(k)}_{pqj}} = \sum_{t=1}^{r_{k+1}} \frac{\partial \mathsf{L}}{\partial \mathcal{G}^{(k)}_{pqt}} \frac{\partial \mathcal{G}^{(k)}_{pqt}}{\partial \mathcal{C}^{(k)}_{pqj}} = \sum_{t=1}^{r_{k+1}} \frac{\partial \mathsf{L}}{\partial \mathcal{G}^{(k)}_{pqt}} \mathbf{B}^{(k)}_{ts}.$$

Assuming i.i.d. gradients with $\mathrm{Var}\left(\frac{\partial \mathsf{L}}{\partial \mathcal{G}^{(k)}_{pqt}}\right) = \sigma^2_{\nabla \mathcal{G}}$, we obtain

$$\mathrm{Var}\left(\frac{\partial \mathsf{L}}{\partial \mathcal{C}^{(k)}_{pqj}}\right) = R_{i+1}\sigma^2_{\nabla \mathcal{G}}\sigma^2_{\mathbf{B}}.$$

To preserve the variance of the backpropagated gradients, we require

$$\sigma^2_{\mathbf{B}} = \frac{1}{R_{i+1}}.$$

Following the principle of Xavier Glorot initialization [9], which balances the forward and backward variance constraints, we take the harmonic mean of the two bounds, yielding

$$\sigma^2_{\mathbf{B}} = \frac{2}{r_{k+1} + R_{k+1}}.$$

Since a zero-mean uniform distribution $\mathcal{U}(-a, a)$ has variance $\mathrm{Var} = a^2/3$, setting $a = \sqrt{6/(r_{k+1} + R_{k+1})}$ makes its variance exactly equal to $\sigma^2_{\mathbf{B}}$, yielding the final form

$$\mathbf{B}^{(k)}_{ij} \sim \mathcal{U}\left(-\sqrt{\tfrac{6}{r_{k+1}+R_{k+1}}}, \sqrt{\tfrac{6}{r_{k+1}+R_{k+1}}}\right), \quad \forall i, j, k,$$

which completes the proof. □

Remark. *The analysis in Theorem 3 is not restricted to Xavier initialization and naturally extends to other variance-preserving schemes. In particular, enforcing forward-pass variance preservation under Kaiming initialization yields* $\mathbf{B}^{(k)}_{ij} \sim \mathcal{U}\left(-\sqrt{\frac{6}{R_{k+1}}}, \sqrt{\frac{6}{R_{k+1}}}\right)$. *Numerical results are provided in Section C.*

Theorem 4. *Let* $g_\phi(\mathbf{v}) : \mathbb{R}^d \to \mathbb{R}$ *be defined as*

$$g_\phi(\mathbf{v}) = \Phi(g_{\phi_1}(v_1) \times_3 \mathbf{B}^{(1)}, \ldots, g_{\phi_d}(v_d) \times_3 \mathbf{B}^{(d)}),$$

where $\mathbf{v} = [v_1, \ldots, v_d]^{\mathrm{T}} \in \mathbb{R}^d$ *denotes the coordinate vector, and each* $\mathbf{B}^{(k)} \in \mathbb{R}^{r_{k+1} \times R_{k+1}}$ *is a fixed basis. Assume for each mode* $k = 1, \ldots, d$, *the following conditions hold:*

- $g_{\phi_k}(\cdot)$ *is an* L_k*-layer MLP with activation function* $\sigma(\cdot)$ *that is* κ*-Lipschitz continuous;*
- *the spectral norm of each weight matrix in* $g_{\phi_k}(\cdot)$ *is bounded by* η*;*
- *the output is bounded:* $\sup_{v_k} \|g_{\phi_k}(v_k)\|_F \le C_k < \infty$.

Then, $g_\phi(\mathbf{v})$ *is globally Lipschitz continuous, i.e.,*

$$|g_\phi(\mathbf{v}) - g_\phi(\mathbf{v}')| \le \delta \|\mathbf{v} - \mathbf{v}'\|_2,$$

where the global Lipschitz constant $\delta = \sqrt{\sum_{k=1}^d \delta_k^2}$, *and* $\delta_k = (\kappa\eta)^{L_k} \cdot \|\mathbf{B}_k\|_2 \cdot \left(\prod_{j \ne k} C_j\right)$.

Proof. For the i-th layer of the k-th MLP, defined as

$$g^{(k)}_i(\mathbf{x}) = \sigma(\mathbf{W}_i \mathbf{x} + \mathbf{b}_i),$$

the Lipschitz constant is bounded by the product of the activation's constant and the affine transformation's constant:

$$L(g^{(k)}_i) \le L(\sigma) \cdot L(\mathbf{W}_i \mathbf{x} + \mathbf{b}_i) \le \kappa \cdot \|\mathbf{W}_i\|_2 \le \kappa\eta.$$

Hence, for an L_k-layer MLP g_{ϕ_k}, the overall Lipschitz constant satisfies

$$L^{(k)}_g \le \prod_{i=1}^{L_k} L(g^{(k)}_i) \le (\kappa\eta)^{L_k}.$$

We then have

$$\begin{aligned}
&\left\|\mathcal{G}^{(k)}_{:v_k:} - \mathcal{G}^{(k)}_{:v'_k:}\right\|_F \\
&= \|g_{\phi_k}(v_k) \times_3 \mathbf{B}^{(k)} - g_{\phi_k}(v'_k) \times_3 \mathbf{B}^{(k)})\|_F \\
&= \|(g_{\phi_k}(v_k) - g_{\phi_k}(v'_k)) \times_3 \mathbf{B}_k\|_F \\
&\le \|g_{\phi_k}(v_k) - g_{\phi_k}(v'_k)\|_F \cdot \|\mathbf{B}_k\|_2 \\
&\le (\kappa\eta)^{L_k} \|\mathbf{B}_k\|_2 \cdot |v_k - v'_k|.
\end{aligned}$$

Let $\mathbf{G}^{(k)}_{v_k} = \mathcal{G}^{(k)}_{:v_k:} \in \mathbb{R}^{r_k \times r_{k+1}}$, $\mathbf{M}_{(\neg k)} = \mathbf{G}^{(k+1)}_{v_{k+1}} \cdots \mathbf{G}^{(d)}_{v_d} \mathbf{G}^{(1)}_{v_1} \cdots \mathbf{G}^{(k-1)}_{v_{k-1}} \in \mathbb{R}^{r_{k+1} \times r_k}$, and denote by $\mathbf{v}'_k = (v_1, \ldots, v_{k-1}, v'_k, v_{k+1}, \ldots, v_d)$ the coordinate vector differing from $\mathbf{v}$ only at the k-th entry. Then,

$$\begin{aligned}
&|g_\phi(\mathbf{v}) - g_\phi(\mathbf{v}'_k)| \\
&= \left|\mathrm{trace}\left(\mathbf{M}_{(\neg k)} \cdot \mathbf{G}^{(k)}_{v_k}\right) - \mathrm{trace}\left(\mathbf{M}_{(\neg k)} \cdot \mathbf{G}^{(k)}_{v'_k}\right)\right| \\
&\le \|\mathbf{M}\|_F \cdot \left\|\mathbf{G}^{(k)}_{v_k} - \mathbf{G}^{(k)}_{v'_k}\right\|_F \\
&\le \prod_{j \ne k} \left\|\mathbf{G}^{(j)}_{v_j}\right\|_F \cdot \left\|\mathcal{G}^{(k)}_{:v_k:} - \mathcal{G}^{(k)}_{:v'_k:}\right\|_F \\
&\le (\kappa\eta)^{L_k} \cdot \|\mathbf{B}_k\|_2 \cdot \prod_{j \ne k} C_j \cdot |v_k - v'_k|.
\end{aligned}$$

Aggregating across all dimensions yields

$$\begin{aligned}
&|g_\phi(\mathbf{v}) - g_\phi(\mathbf{v}')| \\
&\le \sum_{k=1}^d |g_\phi(\mathbf{v}) - g_\phi(\mathbf{v}'_k)| \\
&\le \sum_{k=1}^d (\kappa\eta)^{L_k} \cdot \|\mathbf{B}_k\|_2 \cdot \prod_{j \ne k} C_j \cdot |v_k - v'_k|.
\end{aligned}$$

Finally, applying the Cauchy–Schwarz inequality gives

$$|g_\phi(\mathbf{v}) - g_\phi(\mathbf{v}')| \leq \sqrt{\sum_{k=1}^{d} \left((\kappa\eta)^{L_k} \cdot \|\mathbf{B}_k\|_2 \cdot \prod_{j\neq k} C_j \right)^2} \cdot \|\mathbf{v} - \mathbf{v}'\|_2 ,$$

which completes the proof. □

B. Task-Specific Losses and Settings

In this section, we provide the loss formulations and hyperparameter settings for the four tasks studied in our experiments. Recall that

$$g_\phi(\{\mathbf{v}_k\}_{k=1}^d) = \Phi(g_{\phi_1}(\mathbf{v}_1) \times_3 \mathbf{B}^{(1)}, \ldots, g_{\phi_d}(\mathbf{v}_d) \times_3 \mathbf{B}^{(d)})$$

denotes the RepTRFD reconstruction with learnable parameters ϕ and fixed bases $\{\mathbf{B}^{(k)}\}_{k=1}^d$. The main hyperparameters in our model include the TR rank $[r_1, \ldots, r_d]$, the latent tensor expansion factor β, the frequency parameter ω_0 for the sinusoidal mapping, and the number of layers in each branch network. Each task is formulated as a single optimization problem minimizing a combination of a data fidelity term and an optional regularization term.

Image and Video Inpainting, which aims to reconstruct missing regions from partially observed visual data:

$$\min_\phi \|\mathscr{P}_\Omega(g_\phi(\{\mathbf{v}_k\}_{k=1}^d) - \mathcal{O})\|_F^2 + \gamma_1 \|g_\phi(\{\mathbf{v}_k\}_{k=1}^d)\|_{\mathrm{TV}} + \gamma_2 \|g_\phi(\{\mathbf{v}_k\}_{k=1}^d)\|_{\mathrm{SSTV}},$$

where $\mathcal{O}$ is the observed incomplete data, and $\mathscr{P}_\Omega(\cdot)$ denotes projection onto observed entries. The total variation (TV) is defined along spatial dimensions as $\|\mathcal{X}\|_{\mathrm{TV}} = \|\nabla_{v_1}\mathcal{X}\|_1 + \|\nabla_{v_2}\mathcal{X}\|_1$, and the spatial-spectral TV (SSTV) involves the spectral dimension, defined as $\|\mathcal{X}\|_{\mathrm{SSTV}} = \|\nabla_{v_1}\nabla_{v_3}\mathcal{X}\|_1 + \|\nabla_{v_2}\nabla_{v_3}\mathcal{X}\|_1$. For all modes k, $r_k = 20$ and $\beta = 10$. Frequency parameter ω_0 is set to 90 for color images and videos, and 120 for MSIs and HSIs. Branch layers $[L_1, L_2, L_3]$ are set to $[1, 1, 2]$ for color images and videos, and $[1, 1, 1]$ for MSIs and HSIs. Regularization parameters are set as follows: $\gamma_1 = \gamma_2 = 5 \times 10^{-5}$ for color images; $\gamma_1 = 5 \times 10^{-5}$ and $\gamma_2 = 5 \times 10^{-4}$ for MSIs and videos; $\gamma_1 = 5 \times 10^{-6}$ and $\gamma_2 = 5 \times 10^{-5}$ for HSIs.

Image Denoising, which aims to recover clean images from noisy observations:

$$\min_\phi \|g_\phi(\{\mathbf{v}_k\}_{k=1}^d) - \mathcal{O}\|_F^2 + \gamma_1 \|g_\phi(\{\mathbf{v}_k\}_{k=1}^d)\|_{\mathrm{TV}} + \gamma_2 \|g_\phi(\{\mathbf{v}_k\}_{k=1}^d)\|_{\mathrm{SSTV}},$$

where $\mathcal{O}$ is the observed noisy data. For all modes k, $r_k = 16$ and $\beta = 5$. Frequency parameter ω_0 is set to 120, and branch layers $[L_1, L_2, L_3]$ are $[1, 1, 2]$. Regularization weights are set as $\gamma_1 = \gamma_2 = 10^{-4}$ for MSIs and $\gamma_1 = \gamma_2 = 10^{-5}$ for HSIs.

Image Super-Resolution, which seeks to reconstruct high-resolution images from their low-resolution counterparts:

$$\min_\phi \|\operatorname{Down}(g_\phi(\{\mathbf{v}_k\}_{k=1}^d)) - \mathcal{O}\|_F^2 + \gamma_1 \|g_\phi(\{\mathbf{v}_k\}_{k=1}^d)\|_{\mathrm{TV}},$$

where $\operatorname{Down}(\cdot)$ is the downsampling operator and $\mathcal{O}$ is the low-resolution observation. For all modes k, $r_k = 20$ and $\beta = 10$. Frequency parameter ω_0 is set to 90, branch layers $[L_1, L_2, L_3]$ are $[1, 1, 2]$, and $\gamma_1 = 5 \times 10^{-5}$.

Point Cloud Recovery, which aims to infer continuous point-wise attributes from partially observed point cloud data:

$$\min_\phi \sum_{k=1}^{N} (g_\phi(\mathbf{v}_k) - \mathbf{O}_{k,5})^2,$$

where the observed data $\mathbf{O} \in \mathbb{R}^{N\times 5}$ contains N points, with each row encoding spatial coordinates (x, y, z), color information c, and a scalar value s. Here, $\mathbf{v}_k = (x_k, y_k, z_k, c_k)$ is the input coordinate-color vector of the k-th point, and $\mathbf{O}_{k,5}$ is the corresponding observed scalar value. For all modes k, $r_k = 20$ and $\beta = 3$. Frequency parameter ω_0 is set to 240, and all branches use a single layer.

C. Supplementary Experimental Results

C.1. Additional Ablation Studies

Effectiveness of the Fixed Basis Strategy. To validate the necessity of a fixed basis, we compare our proposed strategy with a variant where the basis matrices are treated as learnable parameters. As illustrated in Fig. S1, although both methods exhibit similar convergence speeds in the early stage, they diverge significantly in later iterations. The learnable basis model reaches a lower peak PSNR and subsequently suffers from performance degradation. This phenomenon suggests that allowing basis matrices to vary introduces excessive degrees of freedom, causing the model to overfit high-frequency noise or drift away from the variance-preserving initialization. In contrast, our fixed basis strategy acts as a structural regularizer, maintaining improved stability and consistently higher reconstruction quality throughout the training process.

Hyperparameter Sensitivity Analysis. We investigate the sensitivity of two key hyperparameters in our framework, the TR rank and the frequency scaling parameter ω_0. Experiments are conducted on the MSI datasets *Toy* and *Face* for denoising with SD $= 0.2$. Fig. S2 presents the variation of PSNR with different values of these hyperparameters. The results indicate that our method is relatively robust to the

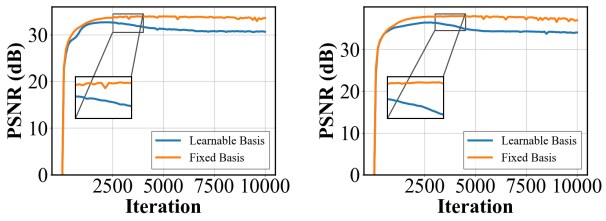

Figure S1. Impact of the fixed basis strategy on denoising performance for the MSIs *Toy* (left) and *Face* (right) with SD $= 0.2$.

choice of both the TR rank and ω_0, maintaining high reconstruction quality across a wide range of settings. In addition, we examine the interaction between the regularization parameter β and the frequency scaling parameter ω_0. As shown in Fig. S3, RepTRFD maintains stable performance over a broad range of parameter combinations.

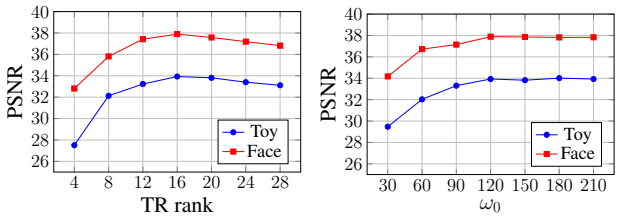

Figure S2. PSNR variation with TR rank and frequency scaling ω_0 for MSI denoising on *Toy* (left) and *Face* (right) datasets with SD $= 0.2$.

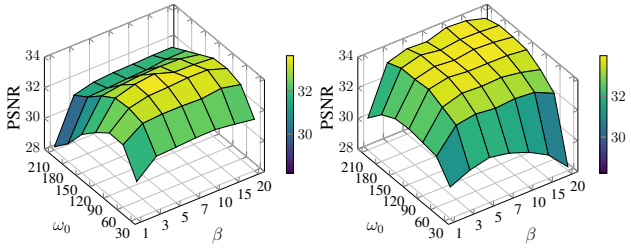

Figure S3. PSNR sensitivity to hyperparameters β and ω_0 for inpainting on *Airplane* (SR $= 0.3$) (left) and denoising on *Toy* (SD $= 0.2$) (right).

Impact of Explicit Regularization. To disentangle the effect of our reparameterized architecture from that of explicit smoothness priors, we further evaluate a variant of RepTRFD trained solely with a data fidelity loss, i.e., without incorporating TV or SSTV regularization. We conduct experiments on both inpainting and super-resolution tasks, contrasting performance against the representative functional tensor baseline, LRTFR [21]. As reported in Tables S1 and S2, even without explicit regularization, our method yields significant PSNR gains over LRTFR across all datasets. This demonstrates the inherent advantage of the proposed reparameterization scheme in capturing latent structures. When regularization is incorporated, performance is further boosted, confirming its complementary role in enhancing spatial smoothness and mitigating artifacts. These results collectively verify that the primary performance improvement stems from the RepTRFD architecture itself, while explicit regularization serves as an effective refinement mechanism.

Table S1. PSNR comparison on image and video inpainting at SR $= 0.2$ under different regularization settings.

Data	LRTFR (Baseline)	RepTRFD (w/o TV)	RepTRFD (w/ TV)
Airplane	27.21	29.37	**30.45**
Flowers	44.27	48.53	**50.13**
Botswana	41.86	44.94	**45.27**
Carphone	30.18	31.86	**32.58**

Table S2. PSNR comparison on $\times 4$ image super-resolution under different regularization settings.

Data	LRTFR (Baseline)	RepTRFD (w/o TV)	RepTRFD (w/ TV)
Lion	28.10	30.37	**31.01**
Parrot	27.81	29.79	**30.39**

Convergence Behavior. To evaluate the effect of the proposed reparameterization on optimization efficiency, we compare the training loss curves of TRFD, LRTFR, and RepTRFD under matched parameter budgets. Fig. S4 shows the training loss curves of TRFD, LRTFR, and RepTRFD under matched parameter settings. RepTRFD converges faster and reaches a lower loss, demonstrating improved convergence behavior.

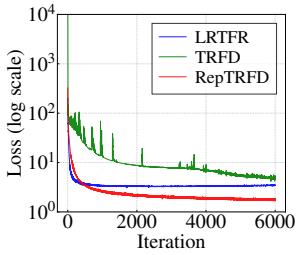

Figure S4. Loss curve on the color image *Airplane* (SR $= 0.3$).

Initialization Scheme. To examine whether the theoretical analysis depends on a specific variance-preserving strategy, we further compare Xavier and Kaiming initialization schemes. Under Kaiming initialization with forward-pass variance preservation, the basis entries follow $\mathbf{B}_{ij}^{(k)} \sim \mathcal{U}\left(-\sqrt{\frac{6}{R_{k+1}}}, \sqrt{\frac{6}{R_{k+1}}}\right)$. Table S3 reports the reconstruction performance on four datasets with SR $= 0.2$. We observe that the two initialization strategies yield highly comparable results across all datasets, with only marginal differences. This indicates that our framework is robust to the specific choice of variance-preserving initialization and that

the theoretical analysis naturally extends beyond Xavier initialization.

Table S3. PSNR results of different variance-preserving initialization schemes on multiple datasets with SR $= 0.2$.

Scheme	*Airplane*	*Toy*	*Botswana*	*News*
Kaiming	30.23	48.59	**45.30**	34.75
Xavier	**30.45**	**48.67**	45.27	**34.90**

C.2. Extended Experimental Results

Extended Inpainting Results. To provide a more comprehensive evaluation, we further include extensive qualitative and quantitative comparisons under various SRs and across diverse data modalities. As shown in Fig. S5, we visualize representative inpainting results on RGB, MSI, HSI, and video datasets, covering a wide range of missing patterns and SRs. The visual comparisons consistently demonstrate that our method yields clearer structural details and fewer artifacts compared to existing approaches. For quantitative evaluation, we report full numerical results of color image inpainting in Table S4, and summarize results on MSI, HSI, and video sequences in Table S5. These results further confirm the robustness and superiority of our method.

Extended Denoising Results. We further conduct denoising experiments on MSI and HSI data under different noise levels, where Gaussian noise with SD ranging from 0.1 to 0.3 is added independently to all pixels and spectral bands. Fig. S6 provides visual comparisons across MSI (*Toys*, *Balloons*) and HSI scenes (*KSC*, *Indian Pines*), showing that our method restores cleaner structural details and yields fewer spectral distortions. Corresponding quantitative results are summarized in Table S6, where PSNR, SSIM, and NRMSE are reported across different SD settings.

Extended Super-Resolution Results. To further demonstrate the generalization ability of RepTRFD in recovering fine structural details under high upscaling factors, we provide additional $\times 4$ visual super-resolution results on the DIV2K dataset, as shown in Fig. S7. Compared with both INR (PEMLP [25], SIREN [37], Gauss [30], WIRE [33], and FINER [17]) and tensor functional representation methods (LRTFR [21]), our approach produces sharper edges, cleaner texture patterns, and fewer artifacts. The quantitative results (PSNR/SSIM) shown above each image further verify the visual comparisons, where RepTRFD consistently achieves the best performance across all samples.

Extended Point Cloud Recovery Results. Fig. S8 presents extended visual results for point cloud recovery under different SRs. We compare the proposed RepTRFD with several INR (PEMLP [25], SIREN [37], Gauss [30], WIRE [33], and FINER [17]) and tensor functional representation methods (LRTFR [21]). Across all tested SRs, our method consistently reconstructs more accurate surface geometry and fine structures, as reflected by the lower NRMSE values shown above each reconstruction. These results demonstrate the superior performance of RepTRFD in point cloud recovery.

Table S4. Quantitative comparison on color images. PSNR, SSIM, and NRMSE are reported under different SRs.

Data	Method	SR = 0.05			SR = 0.1			SR = 0.15			SR = 0.2			SR = 0.25			SR = 0.3		
		PSNR	SSIM	NRMSE	PSNR	SSIM	NRMSE	PSNR	SSIM	NRMSE	PSNR	SSIM	NRMSE	PSNR	SSIM	NRMSE	PSNR	SSIM	NRMSE
Airplane	TRLRF	15.08	0.172	0.218	17.98	0.347	0.156	19.90	0.444	0.125	21.50	0.529	0.104	23.35	0.623	0.084	25.58	0.712	0.065
	FCTN	14.64	0.219	0.229	17.79	0.370	0.159	20.05	0.504	0.123	22.08	0.600	0.097	24.11	0.689	0.077	25.70	0.747	0.064
	HLRTF	18.46	0.396	0.148	21.89	0.598	0.099	24.82	0.746	0.071	26.77	0.811	0.057	27.61	0.795	0.051	29.40	0.852	0.042
	LRTFR	19.66	0.499	0.129	22.09	0.655	0.097	25.57	0.765	0.065	27.21	0.822	0.054	28.60	0.858	0.046	29.38	0.878	0.042
	DRO-TFF	21.08	0.741	0.109	22.71	0.763	0.090	26.28	0.843	0.060	27.64	0.853	0.051	29.17	0.888	0.043	30.37	0.906	0.037
	NeurTV	22.00	0.729	0.098	24.86	0.827	0.071	26.55	0.871	0.058	28.21	0.905	0.048	29.80	0.927	0.040	31.02	0.932	0.035
	Ours	**23.44**	**0.784**	**0.083**	**26.33**	**0.865**	**0.060**	**28.53**	**0.907**	**0.046**	**30.45**	**0.932**	**0.037**	**32.05**	**0.946**	**0.031**	**33.61**	**0.958**	**0.026**
House	TRLRF	15.69	0.208	0.240	17.92	0.360	0.186	20.58	0.520	0.137	22.25	0.617	0.113	23.75	0.694	0.095	25.12	0.751	0.081
	FCTN	15.47	0.248	0.246	18.13	0.424	0.181	19.76	0.545	0.150	20.85	0.619	0.133	22.20	0.681	0.113	24.44	0.756	0.088
	HLRTF	17.93	0.378	0.186	21.48	0.589	0.123	23.93	0.723	0.093	25.40	0.781	0.078	26.76	0.828	0.067	28.19	0.871	0.057
	LRTFR	19.51	0.460	0.155	21.72	0.604	0.120	24.77	0.743	0.084	26.26	0.796	0.071	26.91	0.834	0.066	28.58	0.879	0.054
	DRO-TFF	19.17	0.582	0.161	23.06	0.696	0.103	25.04	0.759	0.082	26.89	0.828	0.066	27.97	0.848	0.058	28.99	0.875	0.052
	NeurTV	21.06	0.651	0.129	23.28	0.761	0.100	25.56	0.820	0.077	26.99	0.856	0.065	28.26	0.881	0.056	29.02	0.910	0.052
	Ours	**22.68**	**0.715**	**0.107**	**25.36**	**0.821**	**0.079**	**27.22**	**0.870**	**0.064**	**28.60**	**0.900**	**0.054**	**29.99**	**0.923**	**0.046**	**30.98**	**0.934**	**0.041**
Pepper	TRLRF	12.97	0.139	0.409	16.83	0.273	0.262	18.77	0.384	0.210	20.99	0.493	0.162	22.92	0.580	0.130	24.23	0.646	0.112
	FCTN	13.86	0.166	0.369	16.24	0.282	0.281	18.82	0.403	0.209	20.90	0.501	0.164	23.02	0.594	0.129	24.37	0.650	0.110
	HLRTF	15.66	0.249	0.300	19.19	0.451	0.200	21.68	0.579	0.150	24.03	0.695	0.114	25.62	0.765	0.095	26.84	0.801	0.083
	LRTFR	15.06	0.289	0.321	20.76	0.537	0.167	22.95	0.655	0.130	24.97	0.720	0.103	26.15	0.767	0.090	27.98	0.796	0.073
	DRO-TFF	18.84	0.502	0.208	23.73	0.730	0.118	26.55	0.824	0.086	28.52	0.871	0.068	30.22	0.906	0.056	31.38	0.923	0.049
	NeurTV	22.14	0.729	0.142	24.69	0.822	0.106	26.99	0.876	0.081	28.73	0.909	0.067	30.37	0.929	0.055	31.46	0.938	0.049
	Ours	**23.14**	**0.755**	**0.127**	**26.10**	**0.854**	**0.090**	**28.02**	**0.878**	**0.072**	**29.82**	**0.919**	**0.059**	**31.29**	**0.935**	**0.050**	**32.46**	**0.945**	**0.043**
Sailboat	TRLRF	15.17	0.197	0.306	17.35	0.324	0.238	19.44	0.438	0.187	21.53	0.547	0.147	22.66	0.606	0.129	24.45	0.683	0.105
	FCTN	14.69	0.209	0.323	17.37	0.362	0.238	18.61	0.434	0.206	21.07	0.545	0.155	22.79	0.631	0.127	24.16	0.687	0.109
	HLRTF	18.12	0.366	0.218	20.98	0.539	0.157	23.07	0.648	0.123	24.86	0.728	0.100	26.35	0.794	0.084	27.66	0.838	0.073
	LRTFR	18.88	0.412	0.200	20.96	0.552	0.157	23.95	0.693	0.111	25.00	0.744	0.099	27.04	0.806	0.078	29.03	0.871	0.062
	DRO-TFF	21.07	0.658	0.155	23.37	0.747	0.119	25.47	0.800	0.093	27.01	0.839	0.078	28.15	0.862	0.069	29.40	0.890	0.059
	NeurTV	21.55	0.663	0.147	23.79	0.778	0.113	25.53	0.819	0.093	27.29	0.865	0.076	28.47	0.888	0.066	29.60	0.916	0.058
	Ours	**22.43**	**0.722**	**0.133**	**25.00**	**0.823**	**0.099**	**27.11**	**0.876**	**0.077**	**28.62**	**0.907**	**0.065**	**29.80**	**0.923**	**0.057**	**31.00**	**0.938**	**0.049**

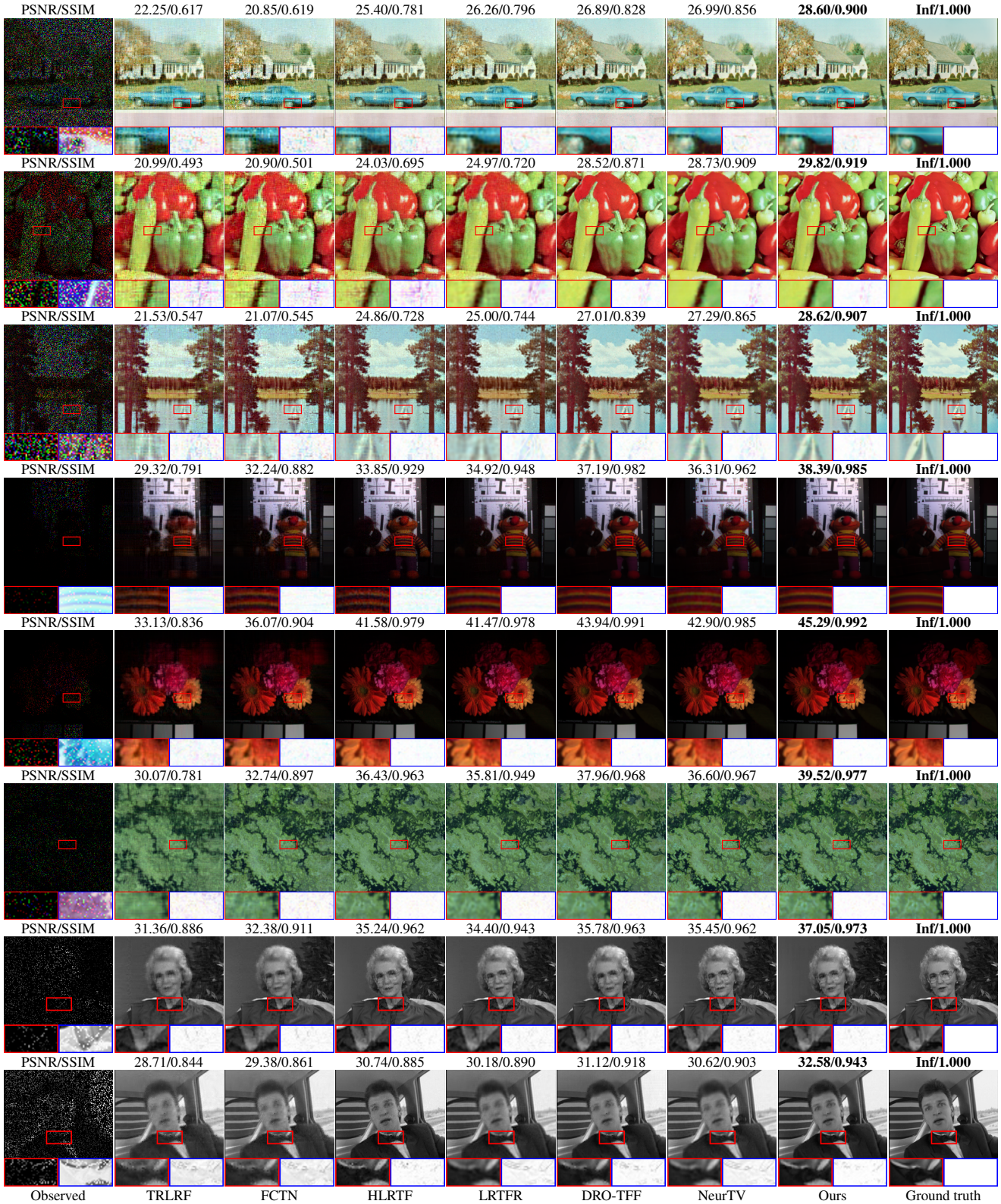

Figure S5. Visual inpainting results on various datasets. From top to bottom: color images (*House*, *Peppers*, *Sailboat*) with SR $= 0.2$; MSIs (*Toy*, *Flowers*) with SR $= 0.05$ and 0.1, respectively; HSI (*Botswana*) with SR $= 0.05$; and video sequences (*Grandma*, *Carphone*) with SR $= 0.1$ and 0.2, respectively.

Table S5. Quantitative comparison on MSIs, HSIs and videos. PSNR, SSIM, and NRMSE are reported under different SRs.

Data	Method	SR = 0.03			SR = 0.05			SR = 0.1			SR = 0.15			SR = 0.2		
		PSNR	SSIM	NRMSE	PSNR	SSIM	NRMSE	PSNR	SSIM	NRMSE	PSNR	SSIM	NRMSE	PSNR	SSIM	NRMSE
Toys ($256 \times 256 \times 31$)	TRLRF	25.13	0.625	0.189	29.32	0.791	0.117	33.67	0.901	0.071	36.56	0.943	0.051	38.67	0.964	0.040
	FCTN	28.22	0.788	0.132	32.24	0.882	0.083	37.46	0.955	0.046	40.04	0.972	0.034	42.04	0.982	0.027
	HLRTF	30.73	0.880	0.099	33.85	0.929	0.069	40.15	0.982	0.033	42.64	0.988	0.025	45.56	0.993	0.018
	LRTFR	32.95	0.924	0.077	34.92	0.948	0.061	39.95	0.982	0.034	41.87	0.987	0.027	43.64	0.988	0.022
	DRO-TFF	33.88	0.966	0.069	37.19	0.982	0.047	40.62	0.992	0.032	43.73	0.994	0.022	45.75	0.995	0.017
	NeurTV	33.34	0.927	0.073	36.31	0.962	0.052	40.43	0.984	0.032	42.31	0.987	0.026	43.09	0.987	0.024
	Ours	**35.16**	**0.972**	**0.059**	**38.39**	**0.984**	**0.041**	**44.04**	**0.993**	**0.021**	**47.16**	**0.995**	**0.015**	**48.67**	**0.996**	**0.011**
Flowers ($256 \times 256 \times 31$)	TRLRF	25.38	0.604	0.318	28.57	0.705	0.220	33.13	0.836	0.130	35.79	0.902	0.096	38.81	0.944	0.068
	FCTN	28.31	0.718	0.227	31.17	0.793	0.163	36.07	0.904	0.093	38.61	0.939	0.069	42.22	0.970	0.046
	HLRTF	30.42	0.830	0.178	35.92	0.945	0.095	41.58	0.979	0.049	44.32	0.988	0.036	46.84	0.992	0.027
	LRTFR	32.64	0.884	0.138	37.84	0.956	0.076	41.47	0.978	0.050	43.10	0.982	0.041	44.27	0.986	0.036
	DRO-TFF	37.09	**0.970**	**0.082**	39.71	0.982	0.061	43.94	0.991	0.038	46.28	0.994	0.029	47.51	0.995	0.025
	NeurTV	35.61	0.934	0.098	38.67	0.966	0.069	42.90	0.985	0.042	45.12	0.990	0.033	46.54	0.992	0.028
	Ours	**37.11**	**0.970**	**0.082**	**40.30**	**0.983**	**0.057**	**45.29**	**0.992**	**0.032**	**48.32**	**0.995**	**0.023**	**50.13**	**0.996**	**0.018**
Washinton DC ($256 \times 256 \times 191$)	TRLRF	26.83	0.635	0.258	29.22	0.771	0.196	32.40	0.914	0.136	35.31	0.954	0.097	37.98	0.973	0.071
	FCTN	28.76	0.830	0.207	32.09	0.912	0.141	34.52	0.946	0.106	36.38	0.963	0.086	41.62	0.987	0.047
	HLRTF	35.31	0.957	0.097	38.29	0.976	0.069	41.68	0.988	0.047	45.04	0.994	0.032	46.66	0.995	0.026
	LRTFR	34.08	0.943	0.112	37.42	0.975	0.076	40.72	0.988	0.052	45.08	0.993	0.032	46.56	0.994	0.027
	DRO-TFF	36.83	0.961	0.082	39.22	0.975	0.062	41.62	0.988	0.047	42.84	0.990	0.041	44.13	0.993	0.035
	NeurTV	35.03	0.950	0.100	38.98	0.977	0.063	44.66	0.992	0.033	46.40	0.993	0.027	47.20	0.995	0.025
	Ours	**38.44**	**0.979**	**0.068**	**41.97**	**0.990**	**0.045**	**45.62**	**0.994**	**0.030**	**47.26**	**0.995**	**0.025**	**47.96**	**0.996**	**0.023**
Botswana ($256 \times 256 \times 145$)	TRLRF	26.89	0.620	0.186	30.07	0.781	0.129	32.08	0.883	0.102	34.12	0.922	0.081	35.49	0.941	0.069
	FCTN	29.32	0.804	0.141	32.74	0.897	0.095	35.36	0.939	0.070	36.22	0.949	0.063	37.70	0.962	0.054
	HLRTF	33.04	0.918	0.092	36.43	0.963	0.062	38.60	0.979	0.048	39.13	0.981	0.045	40.39	0.989	0.039
	LRTFR	32.87	0.906	0.093	35.81	0.949	0.067	37.49	0.964	0.055	40.05	0.980	0.041	41.86	0.986	0.033
	DRO-TFF	34.74	0.945	0.075	37.96	0.968	0.052	40.84	0.981	0.037	41.38	0.982	0.035	42.01	0.984	0.033
	NeurTV	34.23	0.930	0.080	36.60	0.967	0.061	39.32	0.982	0.044	40.25	0.984	0.040	40.74	0.990	0.038
	Ours	**37.11**	**0.965**	**0.057**	**39.52**	**0.977**	**0.043**	**42.81**	**0.987**	**0.030**	**44.40**	**0.990**	**0.025**	**45.27**	**0.992**	**0.022**
News ($144 \times 176 \times 100$)	TRLRF	23.66	0.687	0.180	25.05	0.751	0.153	26.76	0.812	0.126	28.18	0.857	0.107	30.00	0.895	0.087
	FCTN	24.28	0.710	0.168	25.81	0.776	0.141	27.74	0.837	0.113	29.24	0.877	0.095	31.00	0.915	0.077
	HLRTF	25.28	0.811	0.149	26.61	0.842	0.128	29.64	0.914	0.090	31.28	0.937	0.075	32.37	0.949	0.066
	LRTFR	26.15	0.815	0.135	26.63	0.811	0.128	29.62	0.893	0.091	30.58	0.910	0.081	31.86	0.931	0.070
	DRO-TFF	27.91	0.894	0.110	28.89	0.909	0.099	30.66	0.937	0.080	32.28	0.953	0.067	33.02	0.960	0.061
	NeurTV	26.31	0.811	0.133	27.67	0.842	0.113	30.05	0.902	0.086	31.42	0.919	0.074	32.58	0.939	0.064
	Ours	**28.74**	**0.917**	**0.100**	**30.35**	**0.938**	**0.083**	**32.55**	**0.957**	**0.065**	**33.90**	**0.967**	**0.055**	**34.90**	**0.972**	**0.049**
Carphone ($144 \times 176 \times 100$)	TRLRF	22.51	0.607	0.156	24.13	0.680	0.129	26.39	0.769	0.100	27.73	0.816	0.085	28.71	0.844	0.076
	FCTN	23.89	0.663	0.133	25.45	0.729	0.111	27.09	0.792	0.092	28.22	0.831	0.081	29.38	0.861	0.071
	HLRTF	24.28	0.661	0.127	25.71	0.732	0.108	28.12	0.817	0.082	29.63	0.859	0.069	30.74	0.885	0.060
	LRTFR	24.23	0.702	0.128	26.33	0.786	0.100	27.77	0.837	0.085	29.32	0.867	0.071	30.18	0.890	0.064
	DRO-TFF	27.80	0.856	0.085	28.69	0.875	0.076	29.61	0.892	0.069	30.67	0.911	0.061	31.12	0.918	0.058
	NeurTV	25.36	0.709	0.112	27.29	0.793	0.090	28.82	0.847	0.075	29.69	0.894	0.068	30.62	0.903	0.061
	Ours	**28.24**	**0.879**	**0.080**	**29.19**	**0.896**	**0.072**	**30.74**	**0.921**	**0.060**	**31.81**	**0.934**	**0.053**	**32.58**	**0.943**	**0.049**

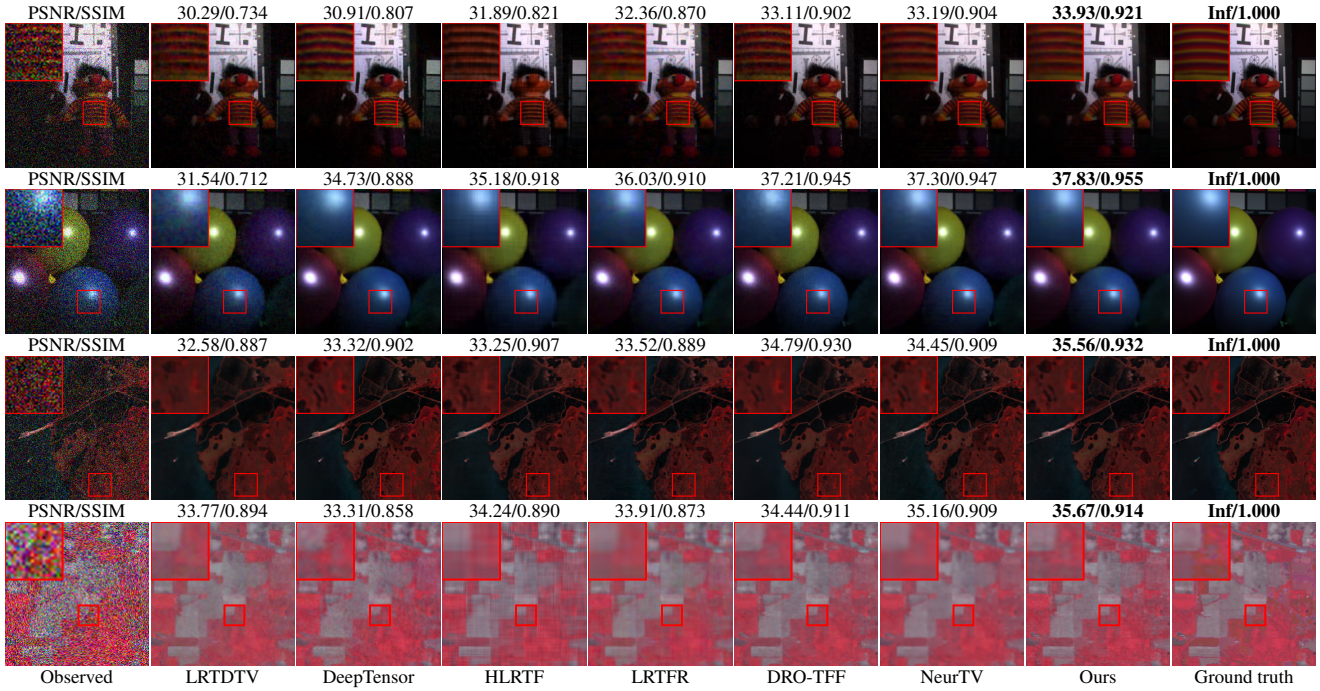

Figure S6. Visual denoising results on MSI *Toy* and *Balloons*, and HSI *KSC* and *Indian Pines* with SD $= 0.2$.

Table S6. Quantitative comparison for denoising under different noise levels. PSNR, SSIM, and NRMSE are reported.

Data	Method	SD $= 0.1$			SD $= 0.15$			SD $= 0.2$			SD $= 0.25$			SD $= 0.3$		
		PSNR	SSIM	NRMSE	PSNR	SSIM	NRMSE	PSNR	SSIM	NRMSE	PSNR	SSIM	NRMSE	PSNR	SSIM	NRMSE
Toys ($256 \times 256 \times 31$)	LRTDTV	34.85	0.906	0.062	32.17	0.824	0.084	30.29	0.734	0.104	28.79	0.653	0.124	27.65	0.581	0.141
	DeepTensor	35.11	0.902	0.060	32.50	0.875	0.081	30.91	0.807	0.097	29.50	0.760	0.114	28.62	0.672	0.126
	HLRTF	35.70	0.912	0.056	33.30	0.883	0.074	31.89	0.821	0.087	30.78	0.768	0.098	29.46	0.698	0.115
	LRTFR	36.01	0.936	0.054	34.01	0.918	0.068	32.36	0.870	0.082	31.36	0.869	0.092	30.60	0.829	0.101
	DRO-TFF	**37.34**	0.954	**0.046**	35.07	0.933	0.060	33.11	0.902	0.075	32.24	0.887	0.083	31.10	0.875	0.095
	NeurTV	36.71	0.951	0.050	35.23	0.920	**0.059**	33.19	0.904	0.075	32.17	0.876	0.084	31.51	0.863	0.091
	Ours	37.25	**0.958**	0.047	**35.30**	**0.941**	**0.059**	**33.93**	**0.921**	**0.069**	**32.89**	**0.902**	**0.077**	**32.04**	**0.889**	**0.085**
Face ($256 \times 256 \times 31$)	LRTDTV	36.85	0.883	0.090	34.11	0.788	0.123	32.26	0.701	0.152	30.55	0.615	0.185	29.24	0.528	0.216
	DeepTensor	37.36	0.926	0.014	35.51	0.904	0.017	34.06	0.859	0.020	32.62	0.814	0.023	31.87	0.732	0.026
	HLRTF	38.49	0.922	0.074	36.40	0.882	0.095	34.67	0.835	0.115	33.37	0.792	0.134	32.30	0.754	0.152
	LRTFR	39.09	0.935	0.069	36.81	0.896	0.090	35.13	0.858	0.109	33.91	0.821	0.126	33.01	0.808	0.140
	DRO-TFF	40.00	0.964	0.062	37.94	0.937	0.079	36.37	0.920	0.095	35.20	0.900	0.109	34.71	0.887	0.115
	NeurTV	40.51	0.968	0.059	38.46	0.949	0.075	36.78	0.927	0.091	35.77	0.914	0.102	35.22	0.902	0.108
	Ours	**40.80**	**0.970**	**0.057**	**39.16**	**0.957**	**0.069**	**37.89**	**0.945**	**0.080**	**36.92**	**0.933**	**0.089**	**36.12**	**0.921**	**0.098**
Washington DC ($256 \times 256 \times 191$)	LRTDTV	34.32	0.924	0.109	32.83	0.896	0.129	31.71	0.869	0.147	30.84	0.845	0.163	30.12	0.823	0.177
	DeepTensor	36.01	0.955	0.090	33.80	0.917	0.116	32.32	0.891	0.137	30.92	0.849	0.161	30.16	0.816	0.176
	HLRTF	36.27	0.959	0.087	34.17	0.927	0.111	32.75	0.913	0.131	31.60	0.892	0.149	30.85	0.879	0.162
	LRTFR	35.78	0.953	0.092	34.22	0.934	0.110	33.02	0.914	0.127	32.09	0.895	0.141	31.34	0.880	0.154
	DRO-TFF	36.65	0.948	0.083	35.26	0.934	0.098	34.26	0.919	0.110	33.35	0.904	0.122	32.57	0.885	0.133
	NeurTV	37.06	0.960	0.079	35.29	0.929	0.097	33.86	0.910	0.115	32.79	0.891	0.130	31.92	0.869	0.144
	Ours	**37.96**	**0.971**	**0.072**	**36.32**	**0.957**	**0.087**	**35.08**	**0.945**	**0.100**	**34.16**	**0.932**	**0.111**	**33.37**	**0.918**	**0.122**
Salinas ($217 \times 217 \times 224$)	LRTDTV	40.13	0.957	0.053	38.19	0.938	0.066	36.82	0.920	0.077	35.83	0.907	0.087	35.01	0.891	0.095
	DeepTensor	40.25	0.952	0.052	38.69	0.938	0.062	37.05	0.921	0.075	36.07	0.902	0.084	35.47	0.896	0.090
	HLRTF	40.20	0.958	0.052	38.85	0.943	0.061	37.50	0.928	0.071	36.52	0.918	0.080	36.06	0.907	0.084
	LRTFR	40.50	0.963	0.051	39.16	0.953	0.059	37.98	0.943	0.068	36.98	0.932	0.076	36.18	0.921	0.083
	DRO-TFF	40.39	0.960	0.051	39.36	0.955	0.058	38.44	0.949	0.064	37.79	0.936	0.069	37.32	0.937	0.073
	NeurTV	41.66	0.966	0.044	40.25	0.961	0.052	39.64	0.954	0.056	38.61	0.939	0.063	37.65	0.930	0.070
	Ours	**42.77**	**0.973**	**0.040**	**41.23**	**0.965**	**0.046**	**40.19**	**0.955**	**0.052**	**39.37**	**0.947**	**0.058**	**38.60**	**0.938**	**0.063**

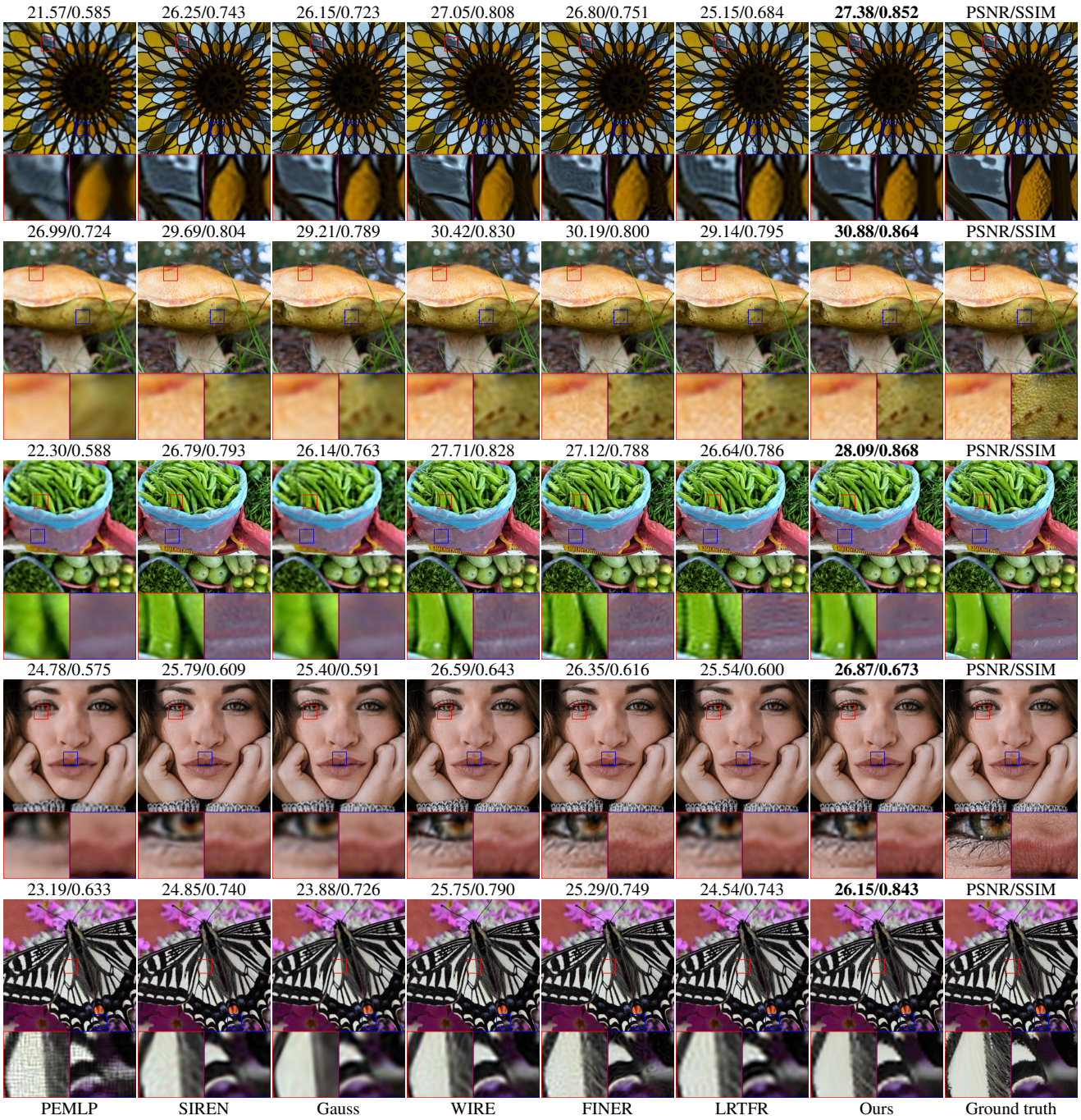

Figure S7. Visual super-resolution results at $\times 4$ scaling on the DIV2K dataset.

Figure S8. Visual comparisons on point cloud recovery over six objects at three SRs: SR $= 0.1$ (*Frog*, *Duck*), SR $= 0.15$ (*PetterRabbit*, *Mario*), and SR $= 0.2$ (*Doll*, *Cola*).